




Cite this: *Nanoscale*, 2025, **17**, 7474

# Proper aggregation of Pt is beneficial for the epoxidation of styrene by O<sub>2</sub> over Pt<sub>x</sub>/γ-Al<sub>2</sub>O<sub>3</sub> catalysts†

Fengfeng Li,‡ Chenyang Shen,‡ Yu He, Haoyu Lu, Rongtian Gu,  Jun Yao, Zhewei Zhang, Feifei Mei, Taotao Zhao, Xiangke Guo, Nianhua Xue and Weiping Ding  \*

The dispersion of metal catalysts has multiple effects on catalytic performance, and higher dispersions do not necessarily imply better performance. Herein, we report the epoxidation reaction of styrene over supported platinum catalysts as an example. Compared with the Pt<sub>1</sub>/γ-Al<sub>2</sub>O<sub>3</sub> catalyst, the Pt<sub>n</sub>/γ-Al<sub>2</sub>O<sub>3</sub> catalyst with a larger Pt cluster size showed a much better performance. Combining the results of various characterizations and density functional theory calculations, Pt<sub>n</sub>/γ-Al<sub>2</sub>O<sub>3</sub> was found to be more favorable for oxygen adsorption and activation to generate singlet oxygen species, further promoting the styrene oxidation reaction to styrene oxide in terms of kinetics. In contrast the metallic center of Pt<sub>1</sub> in Pt<sub>1</sub>/γ-Al<sub>2</sub>O<sub>3</sub> was too small to efficiently activate the diatomic oxygen molecule. These insights provide valuable guidance for designing high-performance metal catalysts.

Received 13th December 2024,

Accepted 7th February 2025

DOI: 10.1039/d4nr05256k

rsc.li/nanoscale

## 1 Introduction

Supported precious metal catalysts offer a broad spectrum of applications in the modern chemical industry, environmental protection, and energy technology. Their effectiveness is closely tied to structural features including particle size, composition, morphology, and metal-support interactions.<sup>1</sup> Particle size, in particular, can fundamentally influence the catalytic performance and availability of active sites within these catalysts.<sup>2,3</sup> Recent developments have highlighted the potential of single-atom catalysts (SACs) for their nearly complete surface exposure of active atoms, which can directly facilitate catalytic reactions.<sup>4–6</sup> However, despite their advantages, the instability and structural variability of SACs limit their practical applications. In response, further research is needed to determine whether single-atom catalysts, nanoparticles or cluster catalysts are more effective for a particular reaction.<sup>7</sup> By carefully adjusting the size,<sup>8,9</sup> shape,<sup>10,11</sup> composition,<sup>12,13</sup> and surface modifications,<sup>14,15</sup> researchers can

significantly alter the electronic properties and surface activity of the catalysts. Such enhancements would not only capitalize on the benefits of extreme dispersion but also improve stability and customization, fostering synergistic interactions at the interface between the active sites and reactants.<sup>16,17</sup> However, achieving uniformity and predictability in the distribution of active sites of supported precious metal catalysts remains challenging despite the advancements made in nanoparticle- and cluster-catalysts in the past decades. Nevertheless, addressing this issue is crucial for maximizing the catalytic efficiency and selectivity in practical applications.

Epoxidation reactions, such as the transformation of styrene into styrene oxide, are crucial for producing essential industrial chemicals used in products like surfactants and resins.<sup>18</sup> The catalytic oxidation of styrene through molecular oxygen presents an environmentally friendly and economically feasible alternative to traditional peroxide-based methods. In this process, molecular oxygen is activated and then converted to reactive oxygen species (ROS), and this procedure is vital for supported heterogeneous catalysts to effectively catalyze the epoxidation of styrene under aerobic conditions.<sup>19</sup> Although many advancements have improved ROS generation, these reactions typically require harsh conditions, such as high temperature or photothermal synergy.<sup>20–22</sup> Multiple mechanisms have been proposed for molecular oxygen activation. One involves the absorption of molecular oxygen at the oxygen vacancies (O<sub>v</sub>) on defective oxide supports.<sup>23–25</sup> Alternatively, the adsorption-dissociation process primarily occurs on noble

Key Lab of Mesoscopic Chemistry, School of Chemistry and Chemical Engineering, Nanjing University, Nanjing 210023, China. E-mail: dingwp@nju.edu.cn

†Electronic supplementary information (ESI) available: Description about catalyst synthesis and characterization method. Results of XRD patterns, nitrogen sorption isotherms, XPS, solvent effects, EXAFS fitting parameters, O<sub>2</sub>-TPD, projected density of state, optimized configurations of O<sub>2</sub> adsorption on the Pt<sub>1</sub>O<sub>2</sub>/γ-Al<sub>2</sub>O<sub>3</sub> and Pt<sub>11</sub>O<sub>18</sub>/γ-Al<sub>2</sub>O<sub>3</sub> model surfaces and the initial, transitional and final states of O<sub>2</sub> dissociation. See DOI: <https://doi.org/10.1039/d4nr05256k>

‡These authors contributed equally.



metal surfaces.<sup>26–28</sup> In this context, platinum (Pt) catalysts are particularly effective owing to their outstanding catalytic activity and efficiency in promoting these activation mechanisms. In general, the particle size of platinum is critical to its catalytic activity since the particle size dictates the amount of active sites on the catalytic surface, thereby influencing the adsorption and activation efficiency of oxygen molecules. Recent studies have underscored the importance of particle size in catalysis, highlighting how its variations can influence the electronic properties and chemical reactivity of the catalyst.<sup>29–31</sup> These studies emphasize the significance of the catalyst size in the activation of molecular oxygen, which is essential for enhancing the epoxidation of styrene and a critical step in this reaction.

Herein, we adopted a facile and effective impregnation strategy to construct catalysts with different Pt sizes to explore the species that can promote the generation of more singlet oxygen species and have a higher selectivity of styrene epoxidation. These Pt catalysts are composed of atomically dispersed Pt at the  $\gamma$ -Al<sub>2</sub>O<sub>3</sub> support (labelled as Pt<sub>1</sub>/γ-Al<sub>2</sub>O<sub>3</sub>) and nanocluster Pt at the  $\gamma$ -Al<sub>2</sub>O<sub>3</sub> support (denoted as Pt<sub>n</sub>/γ-Al<sub>2</sub>O<sub>3</sub>). The latter catalyst in styrene oxidation, in which the dispersion and interaction of Pt with the support is modified by the presence of oleic acid during preparation, shows higher selectivity and activity with reduced metal–support interaction, achieving 81.8% styrene conversion ratio and 70.1% styrene oxide (SO) selectivity, which is more stable compared with the Pt<sub>1</sub>/γ-Al<sub>2</sub>O<sub>3</sub> catalyst. According to the characterizations using X-ray absorption spectroscopy (XAS), aberration-corrected transmission electron microscopy (AC-TEM), as well as density functional theory (DFT) calculations, Pt in Pt<sub>1</sub>/γ-Al<sub>2</sub>O<sub>3</sub> or Pt<sub>n</sub>/γ-Al<sub>2</sub>O<sub>3</sub> catalysts is atomically dispersed or in nanoclusters, respectively. The oxygen activation mechanism over the two catalysts was analyzed through oxygen temperature-programmed desorption (TPD) and *in situ* electron paramagnetic resonance (EPR) measurements, revealing that Pt particle size can influence oxygen activation and overall catalytic performance.

## 2 Results and discussion

### Pt<sub>x</sub>/γ-Al<sub>2</sub>O<sub>3</sub> catalyst texture

Both Pt<sub>1</sub>/γ-Al<sub>2</sub>O<sub>3</sub> and Pt<sub>n</sub>/γ-Al<sub>2</sub>O<sub>3</sub> catalysts were prepared using the incipient wetness impregnation method.<sup>32</sup> Generally, precisely controlling the volume of the precursor solution ensures a thorough coating of the support. Following impregnation, the materials are subjected to drying and calcinating to achieve the final catalyst. For the synthesis of Pt<sub>n</sub>/γ-Al<sub>2</sub>O<sub>3</sub>, an additional step of surface modification is necessary, which alters the interactions between platinum and the support (Fig. S1, ESI†).<sup>33</sup> As shown in Table S1,† the practical loadings of platinum are 0.77 and 0.82 wt% for Pt<sub>1</sub>/γ-Al<sub>2</sub>O<sub>3</sub> and Pt<sub>n</sub>/γ-Al<sub>2</sub>O<sub>3</sub>, respectively, analyzed by ICP, which are close to the theoretical amount (0.80 wt%). Also, compared with bare γ-Al<sub>2</sub>O<sub>3</sub>, sufficient pore volume (~0.50 cm<sup>3</sup> g<sup>−1</sup>) with a high surface area (~130 m<sup>2</sup> g<sup>−1</sup>) is exhibited by both catalysts in

Fig. S3.† Based on the XRD patterns in Fig. S2,† all diffraction peaks of the two catalysts can be indexed to γ-Al<sub>2</sub>O<sub>3</sub> (PDF # 10-0425). The absence of a discernible phase of the platinum-related species is due to the low content and high dispersion of Pt species. HR-TEM images and the corresponding EDS elemental mappings of Pt<sub>1</sub>/γ-Al<sub>2</sub>O<sub>3</sub> and Pt<sub>n</sub>/γ-Al<sub>2</sub>O<sub>3</sub> are shown in Fig. 1. Both the catalysts show similar morphology as the γ-Al<sub>2</sub>O<sub>3</sub> support used. For the Pt<sub>1</sub>/γ-Al<sub>2</sub>O<sub>3</sub> catalyst (in Fig. 1a), no apparent trace of any Pt species can be identified, but the Pt<sub>n</sub>/γ-Al<sub>2</sub>O<sub>3</sub> catalyst (in Fig. 1b) gives evident aggregation of Pt as nanoparticles (NPs) loaded on alumina. The EDS elemental mappings (in Fig. 1c and d) confirm the different dispersion states of the two catalysts.

Due to the intrinsic interactions between the Pt and γ-Al<sub>2</sub>O<sub>3</sub>, the Pt species disperse atomically on the surface of the support (Fig. 2a and b and Fig. S4†). For Pt<sub>n</sub>/γ-Al<sub>2</sub>O<sub>3</sub>, Pt NPs can be observed at low magnification in Fig. 2d, revealing that the weakened metal–support interactions induced the aggregation of Pt atoms. Subsequent statistical analysis also

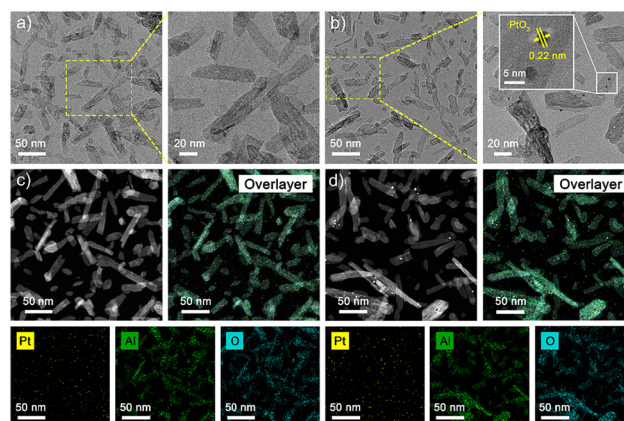


Fig. 1 (a) HR-TEM images of Pt<sub>1</sub>/γ-Al<sub>2</sub>O<sub>3</sub> and (b) Pt<sub>n</sub>/γ-Al<sub>2</sub>O<sub>3</sub>; EDX elemental map distributions of Pt, Al and O of (c) Pt<sub>1</sub>/γ-Al<sub>2</sub>O<sub>3</sub> and (d) Pt<sub>n</sub>/γ-Al<sub>2</sub>O<sub>3</sub>.

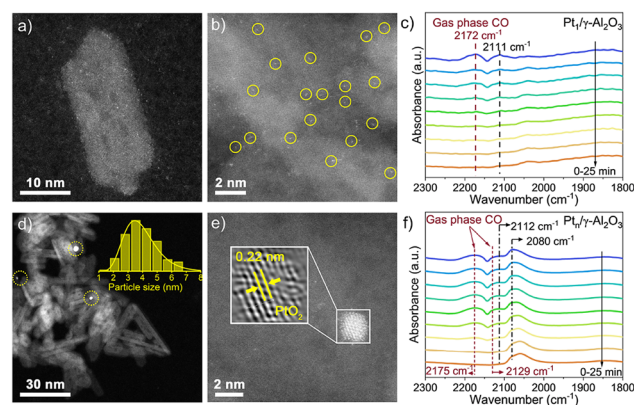


Fig. 2 AC-HAADF-STEM images of Pt<sub>x</sub>/γ-Al<sub>2</sub>O<sub>3</sub> samples. (a and b) Pt<sub>1</sub>/γ-Al<sub>2</sub>O<sub>3</sub>; (d and e) Pt<sub>n</sub>/γ-Al<sub>2</sub>O<sub>3</sub>; *in situ* CO DRIFTS spectra of Pt<sub>x</sub>/γ-Al<sub>2</sub>O<sub>3</sub> samples. (c) Pt<sub>1</sub>/γ-Al<sub>2</sub>O<sub>3</sub> and (f) Pt<sub>n</sub>/γ-Al<sub>2</sub>O<sub>3</sub>.



confirmed that the average size of Pt NCs is *ca.* 3.5 nm. Furthermore, the lattice fringes of 0.22 nm are observed in the metal particle in Pt<sub>n</sub>/γ-Al<sub>2</sub>O<sub>3</sub> (Fig. 1b and 2e), which corresponds to the {111} plane of PtO<sub>2</sub>. The images confirm that Pt species in the Pt<sub>1</sub>/γ-Al<sub>2</sub>O<sub>3</sub> catalyst is atomically dispersed on the γ-Al<sub>2</sub>O<sub>3</sub> support surface, while in the Pt<sub>n</sub>/γ-Al<sub>2</sub>O<sub>3</sub> catalyst, Pt aggregates into nanoparticles and are evenly dispersed on the support.

*In situ* CO diffuse reflectance infrared Fourier transform spectroscopy (CO-DRIFTS) was used to characterize the electronic properties of the two catalysts. The CO band position can be influenced by the particle sizes, surface coverage, and interaction with the support. Fig. 2 shows the CO-DRIFTS spectra of Pt<sub>1</sub>/γ-Al<sub>2</sub>O<sub>3</sub> and Pt<sub>n</sub>/γ-Al<sub>2</sub>O<sub>3</sub> catalysts. Two evident distinctive peaks at 2172 and 2175 cm<sup>-1</sup> in the two catalysts are attributed to gaseous CO.<sup>34</sup> For the Pt<sub>1</sub>/γ-Al<sub>2</sub>O<sub>3</sub> catalyst, discernible peaks within the range of 1700 to 2300 cm<sup>-1</sup> distinctly signify the vibrational and stretching modes associated with the adsorption of CO by Pt sites (Fig. 2c).<sup>35</sup> Moreover, the singular and faint adsorption band manifested at a wavenumber of 2111 cm<sup>-1</sup> implies that CO is linearly bonded to the atomically dispersed Pt sites with a positive charge.<sup>36,37</sup> The CO-DRIFTS spectrum of Pt<sub>n</sub>/γ-Al<sub>2</sub>O<sub>3</sub> catalysts shown in Fig. 2f, except for CO gas adsorption, manifests a novel band positioned at 2080 cm<sup>-1</sup>, indicating CO adsorption on the positively charged Pt<sup>δ+</sup> species, which is a discernible state exclusively presented at the Pt–O–metal interfacial site.<sup>38–40</sup> Throughout the whole purging process, the intensity of these peaks remains consistently stable, revealing the enduring stability of the CO adsorption state on the Pt nanocluster surface. In addition, the CO-DRIFTS results of both the Pt catalysts show the oxidation state of Pt with positive valence.

Further insights into the structure of Pt<sub>1</sub>/γ-Al<sub>2</sub>O<sub>3</sub> and Pt<sub>n</sub>/γ-Al<sub>2</sub>O<sub>3</sub> catalysts were acquired by X-ray absorption fine structure (XAFS) experiments. Pt L<sub>3</sub>-edge X-ray absorption near-edge structure (XANES) spectra shown in Fig. 3a were used to determine the valence state of the Pt species. The corresponding reference spectra of Pt<sub>1</sub>/γ-Al<sub>2</sub>O<sub>3</sub>, Pt<sub>n</sub>/γ-Al<sub>2</sub>O<sub>3</sub>, as well as PtO<sub>2</sub> and Pt foil, are plotted. Thereinto, the Pt<sub>x</sub>/γ-Al<sub>2</sub>O<sub>3</sub> peak (white line) is located between the PtO<sub>2</sub> and Pt foil peaks, which indicates that both atomically dispersed Pt atoms and NPs species are in the form of oxidized platinum. The intensity of the white line for each Pt catalyst is very similar to that of PtO<sub>2</sub>, with a consistent oscillation shape.<sup>41</sup> However, the white line intensity of the Pt nanocluster is higher than that of the Pt SAC, which is shown in an enlarged view in the inset of Fig. 3a, indicating that Pt nanoparticles have a higher valence state, which is consistent with the XPS results. Owing to the overlapping of the Pt 4f peaks with Al 2p,<sup>42</sup> the Pt 4d binding energies were used for the analysis (Fig. S5†). In the two Pt catalysts, Pt species are detected with Pt<sup>2+</sup> and Pt<sup>4+</sup> valence states, while the ratio of Pt<sup>4+</sup>/Pt<sup>2+</sup> in Pt<sub>1</sub>/γ-Al<sub>2</sub>O<sub>3</sub> is significantly higher than that in Pt<sub>n</sub>/γ-Al<sub>2</sub>O<sub>3</sub>. Notably, the oxidized Pt<sup>δ+</sup> peak in the Pt 4d binding energy of Pt<sub>1</sub>/γ-Al<sub>2</sub>O<sub>3</sub> distinctly shifts approximately 0.3 eV lower than that of Pt<sub>n</sub>/γ-Al<sub>2</sub>O<sub>3</sub>. This shift implies electron transfer from the Pt atoms to alumina, attributed to

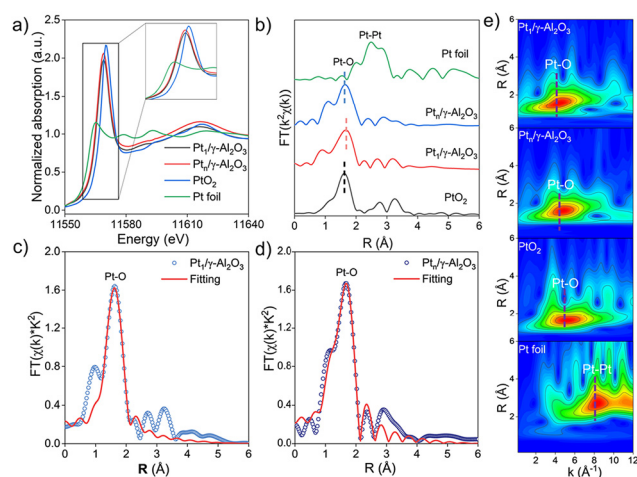


**Fig. 3** (a) Pt L<sub>3</sub>-edge X-ray absorption near-edge structure; (b) Fourier transform EXAFS spectra of Pt<sub>1</sub>/γ-Al<sub>2</sub>O<sub>3</sub>, Pt<sub>n</sub>/γ-Al<sub>2</sub>O<sub>3</sub>, and the corresponding references; (c and d) Fourier transform EXAFS fitting spectrum of Pt<sub>1</sub>/γ-Al<sub>2</sub>O<sub>3</sub> and Pt<sub>n</sub>/γ-Al<sub>2</sub>O<sub>3</sub> at *R* space; (e). Wavelet transform EXAFS of Pt<sub>1</sub>/γ-Al<sub>2</sub>O<sub>3</sub>, Pt<sub>n</sub>/γ-Al<sub>2</sub>O<sub>3</sub>, PtO<sub>2</sub> and Pt foil.

their strong interatomic interactions. It is also proven by the Al 2p peak shown in Fig. S5a.†

Further, we used Fourier-transformed (FT) *k*<sup>2</sup>-weighted extended X-ray absorption fine structure (EXAFS) spectra to analyze the bond lengths and coordination number of Pt species (Fig. 3b). In both Pt<sub>1</sub>/γ-Al<sub>2</sub>O<sub>3</sub> and Pt<sub>n</sub>/γ-Al<sub>2</sub>O<sub>3</sub>, sharp peaks corresponding to the Pt–O layer of coordination at 1.64 Å and 1.68 Å, respectively, are observed, similar to the PtO<sub>2</sub> reference.<sup>43</sup> The least squares method was used to fit the EXAFS spectra to quantify the coordination number of the Pt species (Fig. 2d, e and Table S2†). In both Pt catalysts, there is no Pt–Pt bond, but the Pt–O bond exists, while the Pt–O coordination number is ~5.3 at a distance of 2 Å for Pt<sub>1</sub>/γ-Al<sub>2</sub>O<sub>3</sub> or ~6 at a distance of 1.93 Å for Pt<sub>n</sub>/γ-Al<sub>2</sub>O<sub>3</sub>, respectively. The wavelet transform (WT) analysis is a powerful technique to discern the scattering atoms and provide resolutions in both *R*-space and *k*-space. In Fig. 3e, the WT-EXAFS spectrum of Pt<sub>1</sub>/γ-Al<sub>2</sub>O<sub>3</sub> exhibited a peak at 1.5 Å in the *R* space and 4.4 Å<sup>-1</sup> in the *k*-space, similar to the Pt<sub>n</sub>/γ-Al<sub>2</sub>O<sub>3</sub> catalyst, which showed a maximum at 1.6 Å in the *R* space and 4.3 Å<sup>-1</sup> in the *k*-space, attributable to Pt–O bonds.<sup>44</sup> In contrast, the WT-EXAFS spectrum of the Pt foil displayed a peak at 2.7 Å in the *R* space and 8.3 Å<sup>-1</sup> in the *k*-space in the WT-EXAFS spectrum, corresponding to Pt–Pt bonds.<sup>45</sup> This indicates that Pt atoms were only bonded to oxygen in both catalysts.

Combined with the above systematic characterization analyses, it is discerned that the Pt atoms in both catalysts are in the oxidized state. Notably, the Pt<sub>1</sub>/γ-Al<sub>2</sub>O<sub>3</sub> catalyst was highly dispersed in the form of a single atom, whereas the Pt<sub>n</sub>/γ-Al<sub>2</sub>O<sub>3</sub> catalyst was a nanocluster-type.

### Catalytic performance

The catalytic properties of the Pt<sub>1</sub>/γ-Al<sub>2</sub>O<sub>3</sub> and Pt<sub>n</sub>/γ-Al<sub>2</sub>O<sub>3</sub> samples were explored using styrene epoxidation using O<sub>2</sub> as





the oxidant. Initial optimization revealed that Pt-based catalysts oxidize solvents and reactants simultaneously due to their strong oxidation capabilities. *N,N*-Dimethylformamide (DMF), reported to be an effective solvent for achieving the epoxidation of styrene,<sup>46,47</sup> was utilized to assess the oxidation performance at different temperatures (Fig. S7a and S7b†). However, its strong interaction with the Pt center caused catalyst passivation and low styrene conversion, indicating its unsuitability. Subsequently, other solvents were tested, and it showed that 1,4-dioxane was the best solvent for the reaction (Fig. S7c†). Mannitol was added to prevent the oxidation of 1,4-dioxane at elevated temperatures.<sup>19</sup> To exclude the effect of mass transfer on the reaction kinetics,<sup>48,49</sup> we conducted a series of experiments at different stirring speeds (ranging from 100 rpm to 500 rpm) to assess the effect on catalytic performance. As shown in Fig. S6,† the styrene conversion rate first increased with the stirring speed, reaching a maximum at 300 rpm, and then decreased at higher stirring. Nevertheless, the selectivity of SO mainly decreased with the increase in stirring speed, indicating a shift in the reaction pathway at stirring speeds higher than 300 rpm, which could be due to the disturbance in oxygen transfer and adsorption. Therefore, it was speculated that the reaction kinetics are not significantly affected by mass transfer at 300 rpm, and this stirring speed was chosen for further optimization of the reaction conditions. Fig. 4a and b illustrate that the reaction temperature can influ-

ence the catalytic performance for styrene epoxidation after 10 h. An increase in both styrene conversion ratio and SO selectivity was observed as the reaction temperature rose. Notably, the performance of the Pt<sub>n</sub>/γ-Al<sub>2</sub>O<sub>3</sub> catalyst consistently surpassed that of the Pt<sub>1</sub>/γ-Al<sub>2</sub>O<sub>3</sub> catalyst. As shown in Fig. 4c and d, reaction time can also obviously influence the styrene conversion ratio and SO selectivity, and in this procedure, Pt<sub>n</sub>/γ-Al<sub>2</sub>O<sub>3</sub> maintains superior catalytic activity over the Pt<sub>1</sub>/γ-Al<sub>2</sub>O<sub>3</sub> catalyst. Moreover, as the reaction time extended under 100 °C, the optimum temperature, the reaction rate of both Pt catalysts showed an increasing trend. After 10 hours of the reaction, the Pt<sub>n</sub>/γ-Al<sub>2</sub>O<sub>3</sub> catalyst shows the best catalytic activity, achieving 81.8% styrene conversion and 70.1% selectivity for SO, surpassing the Pt<sub>1</sub>/γ-Al<sub>2</sub>O<sub>3</sub> catalyst, which reached a 65.3% of styrene conversion ratio and 51.5% of SO selectivity. The turnover frequency value for Pt<sub>n</sub>/γ-Al<sub>2</sub>O<sub>3</sub> was confirmed to be 155 h<sup>-1</sup>, which is much higher than that of Pt<sub>1</sub>/γ-Al<sub>2</sub>O<sub>3</sub> (99 h<sup>-1</sup>) in a 3 h reaction (Fig. 4e). The reusability tests showed that Pt<sub>n</sub>/γ-Al<sub>2</sub>O<sub>3</sub> maintained high selectivity and activity over five cycles (Fig. 4f). X-ray diffraction (XRD) patterns of the used catalysts showed no significant changes compared with fresh catalysts, confirming the structural integrity (Fig. S8a†). Furthermore, the size of the Pt nanoparticles remained consistent, as evidenced by the high-resolution transmission electron microscopy (HR-TEM) images (Fig. S8b†).

## Kinetics and mechanism

A kinetic study was performed to clarify the kinetic behaviors and Arrhenius plots for styrene epoxidation on Pt<sub>1</sub>/γ-Al<sub>2</sub>O<sub>3</sub> and Pt<sub>n</sub>/γ-Al<sub>2</sub>O<sub>3</sub> catalysts. According to the various reaction data obtained by the mass transfer and controlling the reaction temperature, the kinetics analysis for the Pt<sub>1</sub>/γ-Al<sub>2</sub>O<sub>3</sub> and Pt<sub>n</sub>/γ-Al<sub>2</sub>O<sub>3</sub> catalysts were processed, which can be linearly plotted against reaction time, as illustrated in Fig. 5a and b. Here, the application of pseudo-first-order kinetics is suitable for assessing the catalytic rate.<sup>50,53</sup> The kinetic equation of this epoxidation reaction may be formulated as follows (eqn (1)):<sup>51</sup>

$$-\ln\left(\frac{C}{C_0}\right) = kt \quad (1)$$

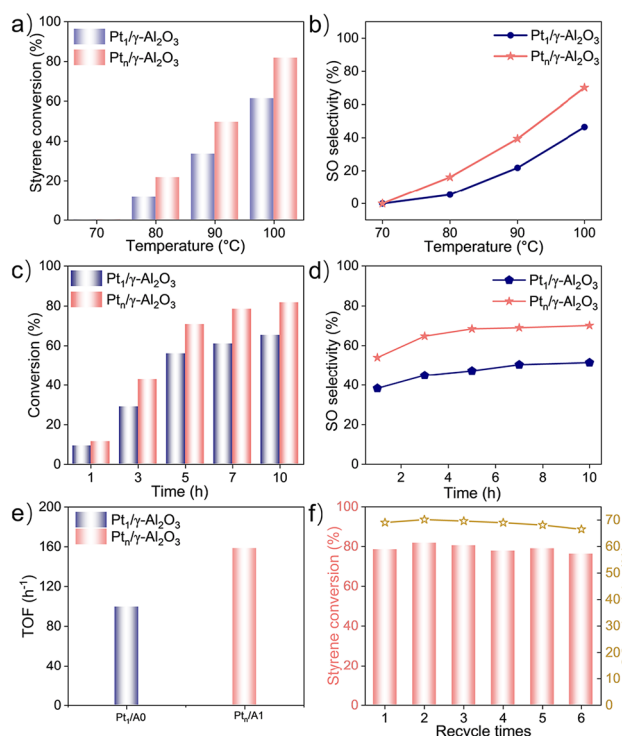


**Fig. 4** Catalytic performance of Pt<sub>1</sub>/γ-Al<sub>2</sub>O<sub>3</sub> and Pt<sub>n</sub>/γ-Al<sub>2</sub>O<sub>3</sub> as a function of (a and b) temperature and (c and d) time; (e) calculated TOF values of Pt<sub>1</sub>/γ-Al<sub>2</sub>O<sub>3</sub> and Pt<sub>n</sub>/γ-Al<sub>2</sub>O<sub>3</sub> for the oxygen of styrene; (f) cyclic stability of Pt<sub>n</sub>/γ-Al<sub>2</sub>O<sub>3</sub>. Reaction conditions: 4.33 mmol styrene, 100 mg catalysts, 20 mL 1,4-dioxane, 1 atm oxygen.

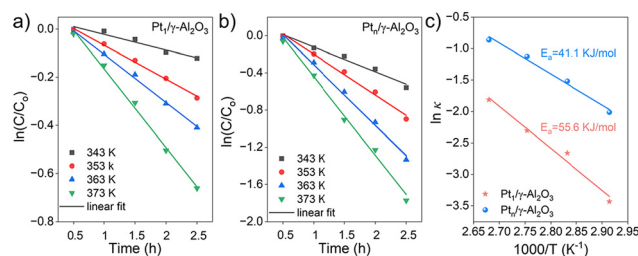


**Fig. 5** Kinetic study of styrene epoxidation by Pt<sub>1</sub>/γ-Al<sub>2</sub>O<sub>3</sub> and Pt<sub>n</sub>/γ-Al<sub>2</sub>O<sub>3</sub> catalysts. (a and b)  $\ln(C/C_0)$  versus reaction time; (c) Arrhenius plots and the calculated apparent activation barriers of styrene epoxidation for Pt<sub>1</sub>/γ-Al<sub>2</sub>O<sub>3</sub> and Pt<sub>n</sub>/γ-Al<sub>2</sub>O<sub>3</sub> catalysts.



where  $t$  is the reaction time;  $C$  is the concentration of the reactants at time  $t$ ;  $C_0$  is the initial concentration of the reactants and  $k$  is the rate constant of the reaction. From the analysis of the slopes in the fitted lines, the calculated rate constants ( $k$  values) for the reactions conducted at different temperatures are listed in Table S3.† The results imply that higher reaction temperature favors faster kinetics, which is consistent with the reaction results.

Based on the results of kinetic analysis, the apparent reaction constants ( $k$ ) were used to calculate the apparent activation energy ( $E_a$ ) in the Arrhenius equation.  $E_a$  can be determined based on the Arrhenius equation (eqn (2)):<sup>53</sup>

$$\ln k = \ln A - \frac{E_a}{RT} \quad (2)$$

where  $A$  is the pre-exponential factor,  $R$  is the molar gas constant ( $8.314 \text{ J K}^{-1} \text{ mol}^{-1}$ ) and  $T$  is the reaction temperature of the epoxidation of styrene. The fitting results and the corresponding  $E_a$  are shown in Fig. 5c.

Compared with  $\text{Pt}_1/\gamma\text{-Al}_2\text{O}_3$ ,  $\text{Pt}_n/\gamma\text{-Al}_2\text{O}_3$  exhibits a higher reaction rate and lower activation energy, as shown in Table S3.† This result further demonstrates that the  $\text{Pt}_n/\gamma\text{-Al}_2\text{O}_3$  catalyst significantly enhances the reaction rate, which is conducive to accelerating the oxidation process of styrene.

The  $\text{O}_2$ -TPD results are depicted in Fig. S9.† Generally, there are three regions of oxygen desorption, respectively, corresponding to the reactive oxygen species ( $\text{O}_2^-/\text{O}^-$ ,  $100\text{--}300^\circ\text{C}$ ), surface lattice oxygen species ( $\text{O}_{\text{latt}}^{2-}$ ,  $350\text{--}500^\circ\text{C}$ ), and bulk lattice oxygen species ( $\text{O}_{\text{latt}}^{2-}$ ,  $500\text{--}700^\circ\text{C}$ ).<sup>52</sup>  $\text{Pt}_n/\gamma\text{-Al}_2\text{O}_3$  shows two peaks at  $376$  and  $475^\circ\text{C}$ , assigned to the adsorbed and lattice oxygen, respectively, while  $\text{Pt}_1/\gamma\text{-Al}_2\text{O}_3$  has only one peak at  $447^\circ\text{C}$ , attributed to the activated lattice oxygen ( $\text{O}_{\text{latt}}^{2-}$ ). The  $\text{Pt}_n/\gamma\text{-Al}_2\text{O}_3$  catalyst exhibits a lower temperature of oxygen desorption and a larger peak area compared to the  $\text{Pt}_1/\gamma\text{-Al}_2\text{O}_3$  catalyst. With the same loading of Pt, the  $\text{Pt}_n/\gamma\text{-Al}_2\text{O}_3$  sample is more active for oxidation.

Fig. 6a shows the catalytic performances of  $\text{Pt}_1/\gamma\text{-Al}_2\text{O}_3$  and  $\text{Pt}_n/\gamma\text{-Al}_2\text{O}_3$  with various quenchers and experimental results

for investigating the mechanism. Firstly, negligible styrene conversion was observed under a nitrogen atmosphere. When 2,2,6,6-tetramethyl-1-piperidinyloxy (TEMPO) was introduced into the system, the reaction was inhibited completely, confirming the ROS-mediated route over the two catalysts. When 1,4-benzoquinone, an efficient  $\text{O}_2^-$  scavenger, was added into the system, the reaction was also shut down, indicative that  $\text{O}_2^-$  is not the main factor affecting SO production. It is interesting that the addition of mannitol (a hydroxyl radical  $\cdot\text{OH}$  trap) cannot change the conversion of styrene and selectivity to SO, which suggests the  $\cdot\text{OH}$  species do not influence styrene epoxidation.<sup>19</sup> However, with the addition of 2,2,6,6-tetramethylpiperidine (TMP, an effective scavenger of  $^1\text{O}_2$ )<sup>53</sup> to the reaction system, the styrene conversion was reduced and SO selectivity was completely inhibited, revealing the singlet oxygen species  $^1\text{O}_2$  is responsible for the styrene epoxidation. *In situ* electron paramagnetic resonance (EPR) spectra were used to monitor the  $^1\text{O}_2$  species over  $\text{Pt}_1/\gamma\text{-Al}_2\text{O}_3$  and  $\text{Pt}_n/\gamma\text{-Al}_2\text{O}_3$  catalysts from  $25^\circ\text{C}$  to  $100^\circ\text{C}$ . As shown in Fig. 6b, a triplet peak with an intensity ratio of  $1:1:1$  was attributed to  $\text{TEMP-}^1\text{O}_2$ . The intensity of the  $^1\text{O}_2$  radical for the  $\text{Pt}_1/\gamma\text{-Al}_2\text{O}_3$  catalyst is very weak, irrespective of the temperature at  $25^\circ\text{C}$  or  $100^\circ\text{C}$ . For the  $\text{Pt}_n/\gamma\text{-Al}_2\text{O}_3$  catalyst, however, an intense EPR signal was observed at  $100^\circ\text{C}$ , though it was weak under  $25^\circ\text{C}$ , indicating that the  $\text{Pt}_n/\gamma\text{-Al}_2\text{O}_3$  catalyst is more conducive to the generation of  $^1\text{O}_2$  driven by heat. These results demonstrate the higher catalytic activity of  $\text{Pt}_n/\gamma\text{-Al}_2\text{O}_3$  compared to  $\text{Pt}_1/\gamma\text{-Al}_2\text{O}_3$ .

### Mechanism elucidated by DFT calculations

We have conducted density functional theory (DFT) calculations to thoroughly understand the mechanism of Pt catalysts with varying sizes for the epoxidation of styrene.

The DFT analyses explored the interaction dynamics between the Pt species and oxygen molecules on  $\gamma\text{-Al}_2\text{O}_3$  surfaces. The optimized configurations of  $\text{Pt}_1\text{O}_2/\gamma\text{-Al}_2\text{O}_3$  and  $\text{Pt}_{11}\text{O}_{18}/\gamma\text{-Al}_2\text{O}_3$  (Fig. 7a and Fig. S10†) revealed significant differences in electronic properties. According to the Bader charge analysis, both Pt catalysts are positively charged. The isolated platinum atom in  $\text{Pt}_1\text{O}_2/\gamma\text{-Al}_2\text{O}_3$  is positively charged with  $+0.78 |e|$ , while more electrons were accumulated on  $\text{Pt}_{11}\text{O}_{18}$ , as shown in Fig. 7b, revealing the platinum atoms in  $\text{Pt}_{11}\text{O}_{18}/\gamma\text{-Al}_2\text{O}_3$  with higher valence, agreeing well with the XPS analysis. In addition, the d-band center upward shift of  $\text{Pt}_{11}\text{O}_{18}$  concerning the Fermi level was observed (Fig. S11†), which may strengthen the bond with oxygen molecules according to the d-band center theory<sup>9</sup> and also benefit the adsorption and activation of molecular oxygen to a certain degree.

Based on the kinetic results,  $\text{O}_2$  activation is the first step within the consecutive styrene oxidation. According to the calculations, the adsorption of oxygen molecules over oxidized platinum NPs ( $-1.24 \text{ eV}$ ) was much stronger than the oxidized platinum single atom ( $-1.89 \text{ eV}$ ) (Fig. S12†). In Fig. 7c, the activation barrier of the adsorbed oxygen ( $\text{O}_2^*$ ) and subsequent dissociation over  $\text{Pt}_1\text{O}_2/\gamma\text{-Al}_2\text{O}_3$  was  $1.38 \text{ eV}$  (II to TS), which is kinetically difficult. By contrast, the reaction occurring on the

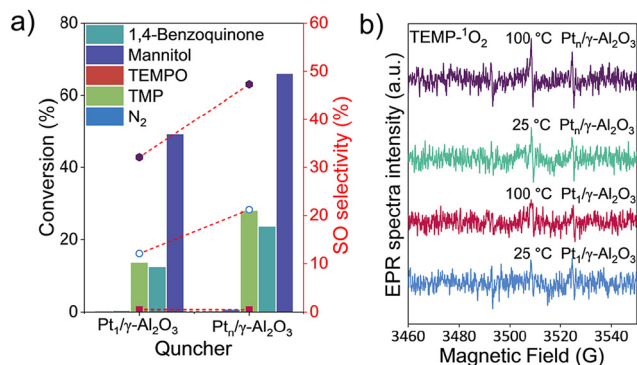
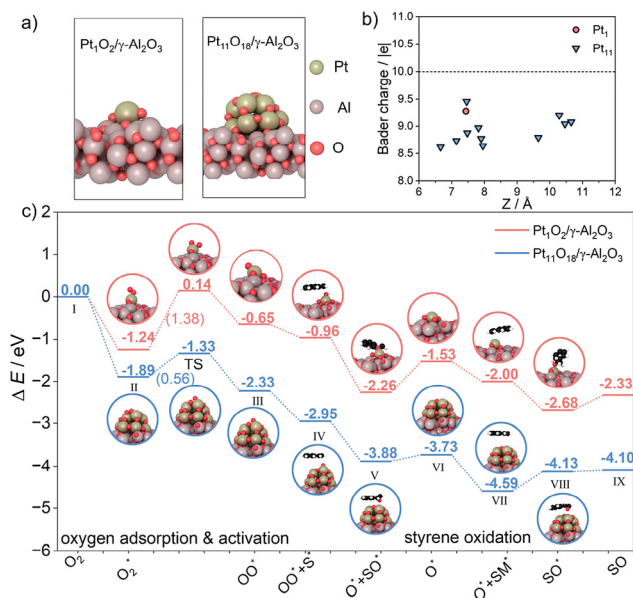


Fig. 6 (a) Catalytic performance of  $\text{Pt}_1/\gamma\text{-Al}_2\text{O}_3$  and  $\text{Pt}_n/\gamma\text{-Al}_2\text{O}_3$  with various quenchers, the red short dash represents the SO selectivity and column represents the styrene conversion; (b) *in situ* EPR spectra of  $\text{Pt}_1/\gamma\text{-Al}_2\text{O}_3$  and  $\text{Pt}_n/\gamma\text{-Al}_2\text{O}_3$  with  $\text{TEMP-}^1\text{O}_2$  at  $25^\circ\text{C}$  and  $100^\circ\text{C}$ .





**Fig. 7** DFT calculations. (a) Optimized configurations of Pt<sub>1</sub>O<sub>2</sub>/γ-Al<sub>2</sub>O<sub>3</sub> and Pt<sub>11</sub>O<sub>18</sub>/γ-Al<sub>2</sub>O<sub>3</sub> models; (b) Bader charge analysis of the platinum atoms in both models. The black dotted line represents the number of valence electrons in platinum; (c) energy profiles of the styrene epoxidation reaction over Pt<sub>1</sub>O<sub>2</sub>/γ-Al<sub>2</sub>O<sub>3</sub> and Pt<sub>11</sub>O<sub>18</sub>/γ-Al<sub>2</sub>O<sub>3</sub>. Color code: Pt (dark golden), Al (brown), O (red), C (black) and H (white).

Pt<sub>11</sub>O<sub>18</sub>/γ-Al<sub>2</sub>O<sub>3</sub> surface (ΔE = −0.44 eV) is thermodynamically favorable with a barrier of 0.56 eV (II to TS), which is easy to overcome. This result indicated that the formation of the O\* species with Pt NPs was far more facile, which is consistent with the EPR results (Fig. 6b). Configurations involved in the initial, transitional and final states are shown in Fig. S13 and S14.†

Along the reaction path, molecular oxygen is firstly adsorbed and activated to the O\* species over both Pt<sub>1</sub>O<sub>2</sub>/γ-Al<sub>2</sub>O<sub>3</sub> and Pt<sub>11</sub>O<sub>18</sub>/γ-Al<sub>2</sub>O<sub>3</sub> and the latter has low exothermic values. Subsequently, a styrene molecule was activated (IV) and transformed to the epoxidation product SO (V), with an energy barrier of −0.93 eV on Pt<sub>11</sub>O<sub>18</sub>/γ-Al<sub>2</sub>O<sub>3</sub> and −1.30 eV on Pt<sub>1</sub>O<sub>2</sub>/γ-Al<sub>2</sub>O<sub>3</sub> (IV to V), which confirmed the Pt<sub>11</sub>O<sub>18</sub>/γ-Al<sub>2</sub>O<sub>3</sub> catalyst with low energy barrier for the epoxidation progress. By overcoming relatively low energy barriers (V to VI), the remaining oxygen is transformed to new one-coordinated oxygen atoms. In this process, Pt<sub>11</sub>O<sub>18</sub>/γ-Al<sub>2</sub>O<sub>3</sub> can more easily overcome the energy barrier of 0.15 eV compared to Pt<sub>1</sub>O<sub>2</sub>/γ-Al<sub>2</sub>O<sub>3</sub>, with a higher energy barrier of 0.73 eV. Subsequently, another new styrene molecule was activated and converted to SO (VII to IX). The energy barrier of Pt<sub>11</sub>O<sub>18</sub>/γ-Al<sub>2</sub>O<sub>3</sub> is just 0.03 eV; however, the Pt<sub>1</sub>O<sub>2</sub>/γ-Al<sub>2</sub>O<sub>3</sub> energy barrier was 0.35 eV, which demonstrated that the SO product is hardly desorbed from the Pt<sub>1</sub>O<sub>2</sub>/γ-Al<sub>2</sub>O<sub>3</sub> catalyst surface. Hence, the DFT calculation results further proved that for the activation of styrene substrates and O<sub>2</sub>, Pt<sub>n</sub>/γ-Al<sub>2</sub>O<sub>3</sub> is the optimum catalyst, while the desorption of SO products is also easier compared to that in Pt<sub>1</sub>/γ-Al<sub>2</sub>O<sub>3</sub>, consistent with the experimental results.

### 3 Conclusions

By precisely tuning the metal–support interaction, the single-atom Pt<sub>1</sub>/γ-Al<sub>2</sub>O<sub>3</sub> and nanocluster-dispersed Pt<sub>n</sub>/γ-Al<sub>2</sub>O<sub>3</sub> catalysts were prepared. Compared with Pt<sub>1</sub>/γ-Al<sub>2</sub>O<sub>3</sub>, the Pt<sub>n</sub>/γ-Al<sub>2</sub>O<sub>3</sub> catalyst exhibited superior catalytic performance for styrene epoxidation. It was confirmed by experimental characterizations and theoretical calculations that Pt<sub>n</sub>/γ-Al<sub>2</sub>O<sub>3</sub> was more active for the activation of O<sub>2</sub> to reactive singlet oxygen species. In addition, owing to its larger size, it offers more sites simultaneously for styrene adsorption and epoxidation at the Pt clusters. Over the Pt<sub>1</sub>/γ-Al<sub>2</sub>O<sub>3</sub> catalyst, however, both the O<sub>2</sub> activation and the desorption energy of styrene oxide show a higher energy barrier. The results provide a comprehensive understanding of the impact of Pt size on the epoxidation of styrene and offer insights into regulation by the metal support for controlling the dispersion and size distribution of platinum on alumina.

### 4 Experimental

#### Catalyst preparation

Reagents used for the catalyst preparation and detailed procedures are described in ESI.†

#### Catalyst characterizations

Catalyst characterization and instruments used as well as specific test methods are given in the ESI.†

#### Catalytic test

The styrene oxidation was conducted in a three-necked glass flask equipped with a reflux condenser. In a typical experiment, styrene, catalysts, and solvent were mixed and added to a 100 mL three-necked glass flask. 1 atm oxygen was then introduced into the system using a balloon. The reaction vessel was conducted at 100 °C in a silicon oil bath with continuous stirring. Once the reactor was cooled to room temperature, the liquid mixture was collected by filtration using a filter membrane (0.22 μm) and then analyzed with a gas chromatography system (GC 9560) connected to a mass detector, in which a known amount of nitrobenzene was introduced as an internal standard. The turnover frequency (TOF) was determined using the following equation (eqn (3)):

$$\text{TOF} = \frac{N_{\text{styrene}} \times C_{\text{styrene}}}{N_{\text{Pt}} \times t} \quad (3)$$

where  $N_{\text{styrene}}$  is the mole number of styrene,  $C_{\text{styrene}}$  is the conversion of styrene,  $N_{\text{Pt}}$  is the total mole number of platinum atoms in the catalyst, and  $t$  is the reaction time (3 h).

The styrene conversion (eqn (4)) and SO selectivity (eqn (5)) was calculated by the following equation:

$$\text{Styrene conversion (\%)} = \frac{\text{converted styrene in molar}}{\text{initial styrene in molar}} \quad (4)$$



$$\text{SO selectivity (\%)} = \frac{\text{SO in the product in molar}}{\text{converted styrene in molar}} \quad (5)$$

### DFT calculations

All spin-polarized DFT calculations were carried out using the Vienna *Ab initio* Simulation Package (VASP 5.4.4),<sup>54,55</sup> a periodic DFT code with projector augmented wave (PAW) potentials. The exchange–correlation energy was described using the generalized gradient approximation (GGA) formulated by the Perdew–Burker–Ernzerhof (PBE) functional.<sup>56</sup> The plane-wave basis sets were converged by a kinetic energy cutoff of 400 eV and a Monkhorst–Pack ( $3 \times 3 \times 1$ ) *k*-point was applied for the sampling of the Brillouin Zone. The convergence criterion of energy and gradient was set as  $10^{-5}$  and  $0.03 \text{ eV \AA}^{-1}$ , respectively. The reaction energy ( $\Delta E$ ) and activation barrier ( $E_a$ ) were defined as the energy difference between the initial state (IS) and final state (FS) and the energy difference between the initial state and transition state (TS), respectively. The transition states were located *via* the climbing-image nudged elastic band (CI-NEB) method<sup>57</sup> together with the improved dimer method (IDM),<sup>58</sup> and finally confirmed by the frequency vibrations. Atomic charges were computed through the Bader charge analysis.<sup>59</sup>

The pristine  $\gamma\text{-Al}_2\text{O}_3(111)$  surface was modelled by a periodic ( $1 \times 1$ ) supercell slab containing three Al–O–Al atomic layers. A vacuum height of 15 Å along the *Z* direction was set between the slab surfaces to eliminate unphysical interactions. During the structural optimization, the atoms in the bottom layer were frozen in the bulk positions while the remaining atoms were fully relaxed. Based on the structural characterizations, two different models were taken into account. As for modelling the single-atom structured platinum, an isolated  $\text{Pt}_1\text{O}_2$  was supported above the  $\gamma\text{-Al}_2\text{O}_3(111)$  surface and named  $\text{Pt}_1\text{O}_2/\gamma\text{-Al}_2\text{O}_3$ . Moreover, platinum oxides with bigger sizes were represented by substituting the  $\text{Pt}_1\text{O}_2$  with an optimized  $\text{Pt}_{11}\text{O}_{18}$  cluster, which was named as  $\text{Pt}_{11}\text{O}_{18}/\gamma\text{-Al}_2\text{O}_3$ .

### Author contributions

F. F. L.: investigation, methodology, data curation, software, writing – original draft. C. Y. S.: software, validation, writing – review & editing. Y. H.: validation. H. Y. L.: validation. R. T. G.: methodology. J. Y.: software, validation. Z. W. Z.: validation, data curation. F. F. M.: writing – review & editing. T. T. Z.: data curation. X. K. G. and N. H. X. review. W. P. D.: conceptualization, funding acquisition, writing – review & editing, supervision.

### Data availability

The authors state that the data included in the current paper are available on request.

### Conflicts of interest

There are no conflicts to declare.

### Acknowledgements

This work was supported by the National Natural Science Foundation of China (21932004, 91963206, 22172072, and 22072090) and the Ministry of Science and Technology of China (2021YFA1500301). The support from the NJU-HUACHANG Joint Institute of Meso Catalysis is also appreciated.

### References

- 1 M. Macino, A. J. Barnes, S. M. Althahban, R. Qu, E. K. Gibson, D. J. Morgan, S. J. Freakley, N. Dimitratos, C. J. Kiely, X. Gao, A. M. Beale, D. Bethell, Q. He, M. Sankar and G. J. Hutchings, *Nat. Catal.*, 2019, **2**, 873–881.
- 2 L. Liu and A. Corma, *Chem. Rev.*, 2018, **118**, 4981–5079.
- 3 A. Okrut, R. C. Runnebaum, X. Ouyang, J. Lu, C. Aydin, S.-J. Hwang, S. Zhang, O. A. Olatunji-Ojo, K. A. Durkin, D. A. Dixon, B. C. Gates and A. Katz, *Nat. Nanotechnol.*, 2014, **9**, 459–465.
- 4 L. Wang, H. Liu, J. Zhuang and D. Wang, *Small Sci.*, 2022, **2**, 2200036.
- 5 Y. Yao, Q. Dong, A. Brozena, J. Luo, J. Miao, M. Chi, C. Wang, I. G. Kevrekidis, Z. J. Ren, J. Greeley, G. Wang, A. Anapolsky and L. Hu, *Science*, 2022, **376**, eabn3103.
- 6 W. Jing, H. Shen, R. Qin, Q. Wu, K. Liu and N. Zheng, *Chem. Rev.*, 2022, **123**, 5948–6002.
- 7 M. Nasrollahzadeh, M. Sajjadi, S. Irvani and R. S. Varma, *J. Hazard. Mater.*, 2021, **401**, 123401.
- 8 J. Hui, H. Chu, W. Zhang, Y. Shen, W. Chen, Y. Hu, W. Liu, C. Gao, S. Guo, G. Xiao, S. Li, Y. Fu, D. Fan, W. Zhang and F. Huo, *Nanoscale*, 2018, **10**, 8772–8778.
- 9 C. Yang, Z. Dao, S. Pu, W. Yan, Y. Wang, D. Tian, C. Min, J. Zhao and C. Zhuang, *ACS Appl. Nano Mater.*, 2024, **7**, 6429–6441.
- 10 F. Xue, Q. Li, M. Lv, Y. Song, T. Yang, X. Wang, T. Li, Y. Ren, K. Ohara, Y. He, D. Li, Q. Li, X. Chen, K. Lin and X. Xing, *J. Am. Chem. Soc.*, 2023, **145**, 26728–26735.
- 11 J. Dou, X. Li, B. Xi, X. Yang, Y. Liu, C. Jin and J. Zhang, *Catal. Sci. Technol.*, 2023, **13**, 5592–5598.
- 12 X. Li, J. Zhang, C. Jin, B. Yan, J. Cai, M. Li, X. Peng and Y. Wang, *ACS Sustainable Chem. Eng.*, 2021, **9**, 11062–11069.
- 13 H. Yang, Y. Wu, Z. Zhuang, Y. Li and C. Chen, *Chin. J. Chem.*, 2021, **40**, 515–523.
- 14 A. Xu, R. Chen, W. Zhao, J. Lin, R. Hu, A. Khan, W. Li, X. Li, S. Zhao and Y. Qiu, *Chem. Eng. J.*, 2023, **473**, 145343.
- 15 W. Zhao, M. Adeel, P. Zhang, P. Zhou, L. Huang, Y. Zhao, M. A. Ahmad, N. Shakoob, B. Lou, Y. Jiang, I. Lynch and Y. Rui, *Environ. Sci.: Nano*, 2022, **9**, 61–80.





- 16 Y. Yu, Q. Zhang, Q. Yao, J. Xie and J. Y. Lee, *Acc. Chem. Res.*, 2014, **47**, 3530–3540.
- 17 H. Lv, W. Guo, M. Chen, H. Zhou and Y. Wu, *Chin. J. Catal.*, 2022, **43**, 71–91.
- 18 A. S. Sharma, V. S. Sharma, H. Kaur and R. S. Varma, *Green Chem.*, 2020, **22**, 5902–5936.
- 19 M. Li, P. Wang, Z. Ji, Z. Zhou, Y. Xia, Y. Li and S. Zhan, *Appl. Catal., B*, 2021, **289**, 120020.
- 20 M. Li, L. Ma, L. Luo, Y. Liu, M. Xu, H. Zhou, Y. Wang, Z. Li, X. Kong and H. Duan, *Appl. Catal., B*, 2022, **309**, 121268.
- 21 F. Li, J. Tang, Q. Ke, Y. Guo, M. N. Ha, C. Wan, Z. Lei, J. Gu, Q. Ling, V. N. Nguyen and W. Zhan, *ACS Catal.*, 2021, **11**, 11855–11866.
- 22 S. Dissanayake, N. Vora, L. Achola, Y. Dang, J. He, Z. Tobin, X. Lu, A. Mirich, P.-X. Gao and S. L. Suib, *Appl. Catal., B*, 2021, **282**, 119573.
- 23 S. Zhao, Y. Yang, F. Bi, Y. Chen, M. Wu, X. Zhang and G. Wang, *Chem. Eng. J.*, 2023, **454**, 140376.
- 24 S. Zhan, H. Zhang, X. Mi, Y. Zhao, C. Hu and L. Lyu, *Environ. Sci. Technol.*, 2020, **54**, 8333–8343.
- 25 L. Hao, H. Huang, Y. Zhang and T. Ma, *Adv. Funct. Mater.*, 2021, **31**, 2100919.
- 26 U. J. Etim, P. Bai, O. M. Gazit and Z. Zhong, *Catal. Rev.*, 2021, **65**, 239–425.
- 27 G. Gao, G. Zhu, X. Chen, Z. Sun and A. Cabot, *ACS Nano*, 2023, **17**, 20804–20824.
- 28 S. Zhang, Z. Tian, Y. Ma and Y. Qu, *ACS Catal.*, 2023, **13**, 4629–4645.
- 29 T. Gan, J. Yang, D. Morris, X. Chu, P. Zhang, W. Zhang, Y. Zou, W. Yan, S.-H. Wei and G. Liu, *Nat. Commun.*, 2021, **12**, 2741.
- 30 Y. Zhuo, X. Guo, W. Cai, T. Shao, D. Xia, C. Li and S. Liu, *Appl. Catal., B*, 2023, **333**, 122789.
- 31 B. Niu, Y. Wang, T. Zhao, X. Duan, W. Xu, Z. Zhao, Z. Yang, G. Li, J. Li, J. Cheng and Z. Hao, *Environ. Sci. Technol.*, 2024, **58**, 4428–4437.
- 32 J. H. Kwak, J. Hu, D. Mei, C.-W. Yi, D. H. Kim, C. H. F. Peden, L. F. Allard and J. Szanyi, *Science*, 2009, **325**, 1670–1673.
- 33 R. Gu, D. Meng, M. She, Y. Wang, H. Yang, X. Guo, N. Xue and W. Ding, *Chem. Commun.*, 2022, **58**, 7630–7633.
- 34 K. Yuan, Y. Guo, Q.-L. Lin, L. Huang, J.-T. Ren, H.-C. Liu, C.-H. Yan and Y.-W. Zhang, *J. Catal.*, 2021, **394**, 121–130.
- 35 M. Kottwitz, Y. Li, R. M. Palomino, Z. Liu, G. Wang, Q. Wu, J. Huang, J. Timoshenko, S. D. Senanayake, M. Balasubramanian, D. Lu, R. G. Nuzzo and A. I. Frenkel, *ACS Catal.*, 2019, **9**, 8738–8748.
- 36 S. Rojas-Buzo, B. Bohigues, D. Salusso, A. Corma, M. Moliner and S. Bordiga, *ACS Catal.*, 2023, **13**, 9171–9180.
- 37 J. Xiong, Y. Wei, Y. Zhang, P. Zhang, Q. Yu, X. Mei, X. Liu, Z. Zhao and J. Liu, *ACS Catal.*, 2020, **10**, 7123–7135.
- 38 V. Matsouka, M. Konsolakis, R. M. Lambert and I. V. Yentekakis, *Appl. Catal., B*, 2008, **84**, 715–722.
- 39 F. Morfin, C. Dessal, A. Sangnier, C. Chizallet and L. Piccolo, *ACS Catal.*, 2024, **14**, 9628–9639.
- 40 C. Dessal, T. Len, F. Morfin, J.-L. Rousset, M. Aouine, P. Afanasiev and L. Piccolo, *ACS Catal.*, 2019, **9**, 5752–5759.
- 41 S. Tian, B. Wang, W. Gong, Z. He, Q. Xu, W. Chen, Q. Zhang, Y. Zhu, J. Yang, Q. Fu, C. Chen, Y. Bu, L. Gu, X. Sun, H. Zhao, D. Wang and Y. Li, *Nat. Commun.*, 2021, **12**, 3181.
- 42 B. A. Riguette, S. Damyanova, G. Gouliev, C. M. P. Marques, L. Petrov and J. M. C. Bueno, *J. Phys. Chem. B*, 2004, **108**, 5349–5358.
- 43 Y. Li, Y. Li, Y. Ding, J. Ma, P. Das, B. Zhang, Z.-S. Wu and X. Bao, *Chem. Catal.*, 2023, **3**, 100658.
- 44 H. Liu, S. Qiang, F. Wu, X.-D. Zhu, X. Liu, J. Yu, Y.-T. Liu and B. Ding, *ACS Nano*, 2023, **17**, 19431–19440.
- 45 L. Shi, Y. Zhou, S. Qi, K. J. Smith, X. Tan, J. Yan and C. Yi, *ACS Catal.*, 2020, **10**, 10661–10671.
- 46 C. Weerakkody, S. Biswas, W. Song, J. He, N. Wasalathanthri, S. Dissanayake, D. A. Kriz, B. Dutta and S. L. Suib, *Appl. Catal., B*, 2018, **221**, 681–690.
- 47 Y. Xiong, W. Sun, P. Xin, W. Chen, X. Zheng, W. Yan, L. Zheng, J. Dong, J. Zhang, D. Wang and Y. Li, *Adv. Mater.*, 2020, **32**, 2000896.
- 48 W. Chen, G. Qian, Y. Wan, D. Chen, X. Zhou, W. Yuan and X. Duan, *Acc. Chem. Res.*, 2022, **55**, 3230–3241.
- 49 W. Chen, W. Fu, X. Duan, B. Chen, G. Qian, R. Si, X. Zhou, W. Yuan and D. Chen, *Engineering*, 2022, **14**, 124–133.
- 50 J.-H. Noh, R. Patala and R. Meijboom, *Appl. Catal., A*, 2016, **514**, 253–266.
- 51 J. Liu, R. Meng, J. Li, P. Jian, L. Wang and R. Jian, *Appl. Catal., B*, 2019, **254**, 124–222.
- 52 Q. Zhao, Y. Gu, H. Fu, X. Qu, Z. Xu, B. Chefetz, S. Zheng and D. Zhu, *Environ. Sci. Technol.*, 2024, **58**, 3483–3494.
- 53 M. Neamtu, C. Nadejde, V. D. Hodoroaba, R. J. Schneider and U. Panne, *Appl. Catal., B*, 2018, **232**, 553–561.
- 54 G. Kresse and J. Furthmüller, *Phys. Rev. B:Condens. Matter Mater. Phys.*, 1996, **54**, 11169–11186.
- 55 G. Kresse and J. Furthmüller, *Comput. Mater. Sci.*, 1996, **6**, 15–50.
- 56 J. P. Perdew, K. Burke and M. Ernzerhof, *Phys. Rev. Lett.*, 1996, **77**, 3865–3868.
- 57 G. Henkelman and H. Jónsson, *J. Chem. Phys.*, 2000, **113**, 9978–9985.
- 58 G. Henkelman and H. Jónsson, *J. Chem. Phys.*, 1999, **111**, 7010–7022.
- 59 R. F. Bader, *Chemt. Rev.*, 1991, **91**, 893–928.

